

# Microwave Emission from Hybridized States in a Semiconductor Charge Qubit

A. Stockklauser,<sup>\*</sup> V. F. Maisi, J. Basset,<sup>†</sup> K. Cujia, C. Reichl, W. Wegscheider, T. Ihn, A. Wallraff, and K. Ensslin  
*Department of Physics, ETH Zürich, CH-8093 Zurich, Switzerland*  
 (Dated: June 20, 2022)

We explore the microwave radiation emitted from a biased double quantum dot due to the inelastic tunneling of single charges. Radiation is detected over a broad range of detuning configurations between the dot energy levels with pronounced maxima occurring in resonance with a capacitively coupled transmission line resonator. The power emitted for forward and reverse resonant detuning is found to be in good agreement with a rate equation model, which considers the hybridization of the individual dot charge states.

The electronic properties of semiconductor nanostructures have been widely studied using transport measurements [1]. More recently, the use of radio and microwave frequency measurement techniques has enabled and stimulated a new generation of experiments [2–4] mostly with superconducting qubits. In similar device geometries the coupling of double quantum dots in carbon nanotubes [5], gate-defined GaAs heterostructures [6, 7], InAs nanowires [8], and graphene [9] to GHz frequency coplanar waveguide resonators has been explored. Photon emission from biased double quantum dots, gain [10] and micromaser action have been observed by pumping a single microwave resonator mode [11, 12].

Here, we experimentally explore inelastic tunneling in a semiconductor double quantum dot capacitively coupled to a transmission line resonator by detecting the microwave radiation emitted in the process. The detection of the weak microwave signals is facilitated by the use of near quantum limited parametric amplifiers [13, 14]. Previous experiments on quantum dots coupled to microwave resonators [5–9] detected mostly polarizability allowing to extract charge stability diagrams. Here, we demonstrate that the level separation of hybridized states in a double quantum dot, if on resonance with the microwave resonator, can be investigated with high precision by directly detecting inelastic transitions. In particular, the tunneling rates, which are typically difficult to measure in pure dc transport experiments, are directly reflected in the power of the respective emitted microwave radiation. Future options include the possibility to characterize the classical and quantum properties of radiation emission from semiconductor nanostructures at microwave frequencies using correlation function measurements [15] or state tomography [16].

The hybrid device explored in our experiments is realized by capacitively coupling a gate-defined double quantum dot (DQD) to an on-chip superconducting coplanar waveguide resonator [Fig. 1]. The gate structure depicted in Fig. 1(b) is patterned on top of a GaAs/AlGaAs heterostructure with a two-dimensional electron gas (2DEG) 90 nm below the surface. The quantum dots are formed by negatively biasing the top gates. The left and right plunger gates (LPG/RPG) control the electrochemical potentials ( $\epsilon_L/\epsilon_R$ ) of the electrons in the respective dots

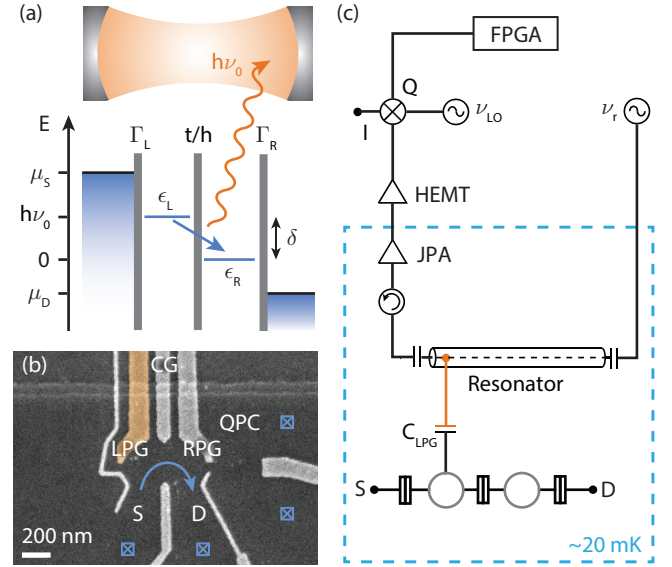


FIG. 1. (a) Energy level structure of a double quantum dot with levels  $\epsilon_L$  and  $\epsilon_R$ . The dots are tunnel coupled to source (S) and drain (D) with chemical potentials  $\mu_S$  and  $\mu_D$  at rate  $\Gamma_L$  and  $\Gamma_R$ . The interdot coupling rate is given by  $t/h$ . We consider the creation of photons in a cavity of resonance frequency  $\nu_0$  in dependence on the interdot detuning  $\delta = \epsilon_L - \epsilon_R$ . (b) Scanning electron micrograph of the quantum dot gates as described in the text. The gate shaded in orange capacitively couples the left dot to the resonator ( $C_{LPG}$ ). (c) Schematic of sample and measurement setup. A coherent microwave signal ( $\nu_r$ ) is applied to the resonator. The output signal passes a circulator, is amplified by a JPA and a HEMT amplifier and finally mixed with an LO signal ( $\nu_{LO}$ ) in a heterodyne detection scheme and processed with an FPGA as discussed in the text.

and thereby the detuning energy  $\delta = \epsilon_L - \epsilon_R$  between the dot levels. The center gate (CG) is used to adjust the interdot tunnel coupling energy  $t$ . The tunnel coupling leads to a hybridization of the left and right dot states. The resulting bonding and antibonding states form a two-level system with an energy separation  $h\nu_q = \sqrt{(2t)^2 + \delta^2}$ , where  $h$  is Planck's constant and  $\nu_q$  denotes the transition frequency of the charge qubit [17].

The 200 nm thick Al coplanar waveguide resonator has

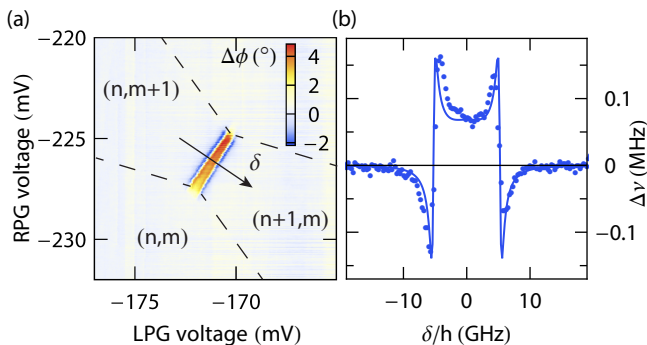


FIG. 2. (a) Change in phase  $\Delta\phi$  of a constant RF measurement tone applied to the resonator as a function of left and right plunger gate voltages (LPG, RPG) in the vicinity of the triple points. The borders between stable charge configurations with  $n$  electrons in the left and  $m$  electrons in the right dot are indicated by dashed lines. The arrow indicates the axis along which the detuning  $\delta$  between the dots is varied. A fluctuating background constant in LPG voltage is subtracted. (b) Associated shift in the resonance frequency  $\Delta\nu = \nu - \nu_0$  against detuning  $\delta$ . The solid line is a Master equation simulation of a Jaynes-Cummings model from which the coupling strength  $g/2\pi \approx 13$  MHz, decoherence rate  $\gamma/2\pi = 250$  MHz and tunnel coupling  $2t/h \approx 4.4$  GHz are extracted [6, 7].

a bare resonance frequency of  $\nu_0 = 6.852$  GHz ( $28 \mu\text{eV}/h$ ) and a loaded quality factor of 2058. The center conductor of the resonator extends to the left dot forming the plunger gate shaded in orange, which mediates dipole coupling between DQD and resonator [Fig. 1(c)] [6, 7]. The sample is similar to the devices presented in Refs. 6 and 18.

We first characterize the properties of the coupled system in microwave transmission measurements as described in Ref. 6. This yields all parameter values relevant for the analysis of the photon emission data presented subsequently. A microwave tone of constant frequency  $\nu_r$  is transmitted through the resonator. The output field is first amplified by a Josephson parametric amplifier (JPA) [19] providing quantum limited amplification [13, 14]. A high electron mobility transistor (HEMT) amplifier provides a second amplification stage before the signal is mixed with a local oscillator (LO) microwave signal. The signal is subsequently digitally down-converted and processed with a field-programmable gate array (FPGA), giving access to its amplitude  $A$  and phase  $\phi$  [Fig. 1(c)] [2].

Charge delocalization between the dots leads to a dispersive frequency shift of the cavity seen as a change in phase  $\Delta\phi$  of the transmitted tone as plotted in Fig. 2(a). The charge stability regions are indicated together with the  $\delta$ -axis along which the detuning between the dots is varied [20]. In the presented experiments, the number of electrons in each dot is on the order of 10 as deter-

mined by quantum point contact (QPC) charge detection [21, 22].

The dispersive frequency shift as a function of  $\delta$  is measured by recording full transmission spectra. At detuning energies in the vicinity of the qubit-cavity resonance condition the resonator frequency is strongly shifted [Fig. 2(b)]. We calculate the frequency shift numerically using a Jaynes-Cummings model [23] to extract the resonator-dot coupling strength  $g$ , the interdot tunnel coupling energy  $t$  and the decoherence rate  $\gamma$ . To analyze the emission experiments performed at different tunnel coupling energies  $t$  discussed in the following, we have used a constant value of  $g/2\pi \approx 11$  MHz, see Ref. 24.

With this device, decoherence rates as low as  $250 \pm 50$  MHz were observed, which is more than an order of magnitude lower than for previous samples investigated in our group [6, 18] and comparable to the lowest rates observed in other experiments [7, 25, 26]. We attribute the improvement to a combination of optimized filtering and a very stable 2DEG. It also manifests itself in a reduced electron temperature of  $\sim 60$  mK as extracted from conductance resonances. Note that the improved coherence facilitates the emission experiments presented below.

To study photon emission from the double dot, we apply a bias of  $V_{\text{SD}} = -200 \mu\text{V}$  (48 GHz) between source and drain. The bias is chosen to be smaller than both the charging energies and the single-particle level spacing to ensure single-level transport. The charging energy of each dot is roughly 1 meV ( $\approx 200 \text{ GHz} \cdot h$ ), as extracted from the stability diagram, and at  $V_{\text{SD}} = -200 \mu\text{V}$  transport measurements show no excited states in the bias window. The tunnel coupling to the leads, adjusted to  $\Gamma_L \approx \Gamma_R \sim 1$  GHz, controls the current through the device.

We measure the power spectral density (PSD) of photons emitted from the cavity [24, 27] with the DQD being the only source of radiation. For detuning values  $|\delta/h|$  larger than the resonance frequency, we find a low photon signal of less than  $0.01 \text{ Hz}^{-1}\text{s}^{-1}$ , see purple curve in Fig. 3(a). Close to resonance, the photon signal is significantly increased to more than  $0.06 \text{ Hz}^{-1}\text{s}^{-1}$  (red curve) corresponding to an average number of 0.015 photons in the resonator extracted from the integrated PSD. Both data sets fit well to a Lorentzian lineshape (solid lines) taking into account the frequency dependence of the parametric amplifier gain. The linewidths extracted from all PSD measurements are identical to the resonator linewidth  $\kappa/2\pi = 3.3$  MHz.

We measure the PSD vs. detuning  $\delta$  around the lower triple point shown in Fig. 2(a). The detuning between the dots is positive when it is in forward direction with respect to the applied bias [Fig. 4(c)]. Integrating Lorentzian fits to the data yields the number of photons emitted from the cavity per unit of time,  $P$ . The

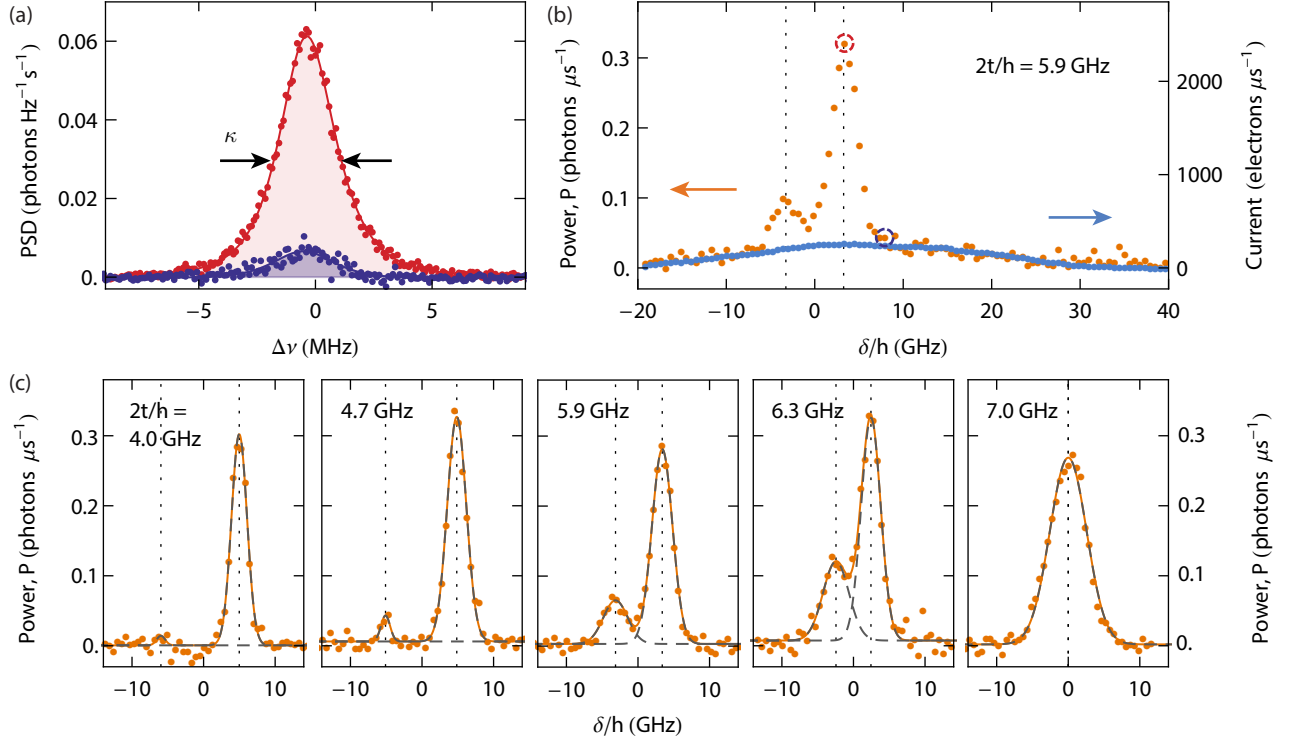


FIG. 3. (a) Power spectral density (PSD) of microwave emission measured at the two detuning energies  $\delta$  indicated by dashed circles in (b). The extracted linewidth corresponds to the resonator linewidth  $\kappa$ . (b) Plot of the source drain current (blue, scale on the right hand side) and the emission power in units of photons emitted into the cavity per microsecond (orange) against detuning  $\delta$ . Each point in emission power is obtained by integrating the respective PSD. (c) Photon emission power measured for the indicated interdot tunnel rates  $2t/h$ . The background proportional to the current is subtracted and the emission resonances are fitted using a sum of two Gaussian lineshapes to extract the values of resonant detuning and power (sum: solid orange line; individual lineshapes: dashed gray lines).

power  $P$  is plotted in Fig. 3(b) as a function of detuning  $\delta$  (orange) and compared to the simultaneously measured source-drain current (blue). We observe a pronounced resonance in the measured power  $P$  at positive detuning ( $+\delta_0$ ) as well as a lower peak at negative detuning ( $-\delta_0$ ). These maxima occur when the energy released in the interdot transition corresponds to the resonator frequency ( $\nu_q = \nu_0$ ) yielding the resonant detuning energies

$$\pm\delta_0 = \pm\sqrt{(h\nu_0)^2 - (2t)^2}. \quad (1)$$

The background emission power away from the resonances is proportional to the current. We associate it with combined photon/phonon processes and tunneling processes between the left or right dot and the continuum of states in the leads. The proportionality factor is the same for all measurements and yields a background rate of roughly  $1.3 \times 10^{-4}$  photons emitted from the cavity per transported electron. This shows that competing relaxation channels for the qubit, such as phonon emission, are relevant in inelastic processes even in the presence of the resonator [10, 28, 29].

We investigate emission for interdot tunnel coupling rates up to  $2t/h = 7.4 \text{ GHz}$ . Representative examples

are shown in Fig. 3(c). We find that the emission power at  $-\delta_0$  increases with  $t$ , while the separation between the resonances, indicated by vertical dashed lines, decreases. To analyze the resonances in emission in detail we subtract the background signal proportional to the current. A sum of two Gaussian lineshapes is fitted to the resonances to analyze the maximum power and resonant detuning [Fig. 3(c)]. We define the zero detuning to be centered between the resonances. For details of the PSD measurement and the extraction of the tunnel coupling, refer to the supplemental material [24].

The extracted resonant detuning  $|\delta_0|/h$  approaches zero as  $2t$  approaches  $h\nu_0$  [Fig. 4(a)]. For  $2t \geq h\nu_0$ , we find a single resonance [Fig. 3(c)], which decreases in power and eventually vanishes when  $t$  is further increased. For  $2t/h < 4 \text{ GHz}$  the emission power at  $-\delta_0$  is below the noise level of our detection system for the chosen integration time, so that no points can be acquired in this region. The experimental data are well described by Eq. (1) and deviations lie within the error margins [Fig. 4(b)] where all parameters are directly determined from the experiment.

For the negative resonance condition  $-\delta_0$ , the detun-

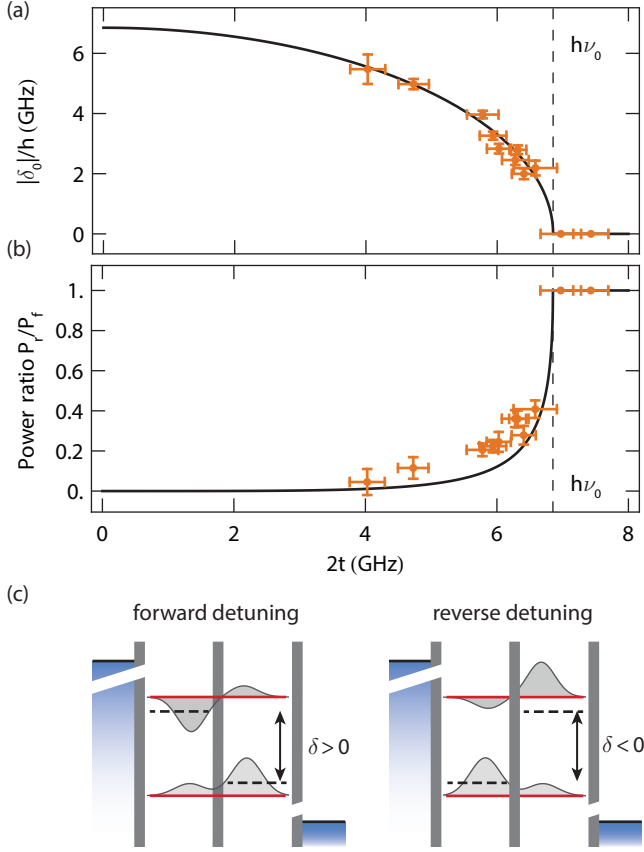


FIG. 4. (a) Resonant detuning  $|\delta_0|$  and (b) power ratio  $P_r/P_f$  as a function of tunnel coupling  $2t$ . The data are compared to expressions (1) and (5) (solid curves). Error bars in  $|\delta_0|$  and  $P_r/P_f$  are determined by fitting error of the Gaussian lineshapes shown in Fig. 3(c), error bars in  $2t$  result from the Jaynes-Cummings simulations of transmission measurements. (c) Level diagrams depicting the wavefunctions of the hybridized dot states for positive and negative detuning. The dashed black lines represent the dot energy levels in the left-right ( $|L\rangle, |R\rangle$ ) basis, the solid red lines represent the hybridized states and the shaded gray areas the wavefunctions of the bonding and antibonding state.

ing of the electronic states is reversed with respect to the source-drain bias [Fig. 4(c)]. In this configuration, transport is expected to be blocked if the hybridization of the occupation states  $|L\rangle, |R\rangle$  of the left and right dots is not considered. The hybridized states are given by

$$|e\rangle = \cos(\theta/2)|L\rangle + \sin(\theta/2)|R\rangle, \quad (2)$$

$$|g\rangle = \sin(\theta/2)|L\rangle - \cos(\theta/2)|R\rangle, \quad (3)$$

where  $\theta$  is given by  $\sin(\theta/2) = \sqrt{(h\nu_q + \delta)/(2h\nu_q)}$ . Considering the antibonding wavefunction  $|e\rangle$ , we find the electron in the left dot with probability  $\alpha = \cos^2(\theta/2)$ , which is a measure of the hybridization of the qubit states [Fig. 4(c)]. Even for reverse detuning, electrons can therefore tunnel into the excited state leading to photon emission at  $-\delta_0$ .

We find that emission power for forward detuning  $P_f$  is roughly independent of  $t$  while photon emission for reverse detuning  $P_r$  increases with  $t$  [Fig. 3(c)]. The power ratio  $P_r/P_f$  approaches unity as  $2t$  approaches  $h\nu_0$  and the peaks merge [Fig. 4(b)].

We model the behavior of the emitted power with increasing  $t$  using a master equation approach. We describe the system by three possible states: qubit in the excited state  $|e\rangle$  (excess electron in antibonding state), qubit in ground state  $|g\rangle$  (excess electron in bonding state) and qubit in state  $|0\rangle$ , which we define as the state with no excess electrons in the dots. This describes the system around the lower triple point. For the upper triple point, the third qubit state corresponds to two extra electrons in the dots leading to the same result. We arrive at the following rate equation for the occupation probabilities of the three qubit states [30]:

$$\begin{cases} \dot{p}_0 = -\Gamma_L p_0 + \alpha\Gamma_R p_g + (1-\alpha)\Gamma_R p_e \\ \dot{p}_g = (1-\alpha)\Gamma_L p_0 - \alpha\Gamma_R p_g - (1-\alpha)\Gamma_R p_e \\ \dot{p}_e = \alpha\Gamma_L p_0 - (1-\alpha)\Gamma_R p_e \end{cases} \quad (4)$$

Here, we neglect the relaxation rate  $\gamma_1$  from the excited to the ground state. This is justified because we estimate  $\gamma_1 \approx 100$  MHz [31], which is significantly smaller than the tunneling rates to the leads  $\Gamma_L \approx \Gamma_R$ . The same holds for the resonator-dot coupling  $g \approx 11$  MHz. We confirmed that including  $\gamma_1$  in the rate equation does not significantly influence the power ratio even for  $\gamma_1 \gg 100$  MHz.

Because the resonant emission signal is generated in transitions from the excited state we expect the emission power to be proportional to  $p_e(\delta)$ , which is obtained using the steady-state condition  $\dot{p} = 0$ . This yields the emission power ratio

$$\frac{P_r}{P_f} = \frac{p_e(-\delta_0)}{p_e(+\delta_0)} = \frac{(h\nu_0)^2 - 2t^2 + h\nu_0\delta_0}{(h\nu_0)^2 - 2t^2 - h\nu_0\delta_0}. \quad (5)$$

The experimental results are well approximated by this model [black solid line in Fig. 4(b)]. There is, however, a systematic deviation, such that the power ratios in all experimental data are slightly higher than the model predicts. We can account for this deviation by considering energy dependent tunnel rates  $\Gamma_L$  and  $\Gamma_R$ , see Ref. 24. Note that, as for the resonant detuning [Fig. 4(a)], there is no free fitting parameter.

In conclusion, we investigated photon emission from a biased double quantum dot dipole coupled to a microwave cavity. We clearly distinguish between background emission and resonant photon emission of the qubit generated in inelastic interdot transitions. We found photon emission for both forward and reverse interdot detuning with respect to source-drain bias reflecting the distribution of wavefunctions in the hybridized electronic states. We modeled the results using a master

equation approach for the DQD and found good agreement with the experiment. In future experiments, microwave correlation function measurements could be used to investigate photon statistics [15, 32]. For the low photon rates we detect from single-electron interdot transitions in our experiments photon antibunching is predicted [33].

We thank C. Eichler for valuable advice, A. Hamblitz for contributions to device fabrication, and C. Lang and Y. Salathé for their support. This work was financially supported by the Swiss National Science Foundation through the National Center of Competence in Research "Quantum Science and Technology" and by ETH Zurich.

---

\* anna.stockklauser@phys.ethz.ch

† now at Laboratoire de Physique des Solides, Univ. Paris-Sud, CNRS, UMR 8502, F-91405 Orsay Cedex, France, julien.basset@u-psud.fr

- [1] C. W. J. Beenakker and H. van Houten, in *Solid State Physics* **44**, 1 (Academic Press, Inc., 1991).
- [2] A. Wallraff, D. I. Schuster, A. Blais, L. Frunzio, R.-S. Huang, J. Majer, S. Kumar, S. M. Girvin, and R. J. Schoelkopf, *Nature* **431**, 162 (2004).
- [3] R. J. Schoelkopf and S. M. Girvin, *Nature* **451**, 664 (2008).
- [4] S. M. Girvin, M. H. Devoret, and R. J. Schoelkopf, *Phys. Scr.* **T137**, 014012 (2009).
- [5] M. R. Delbecq, V. Schmitt, F. D. Parmentier, N. Roch, J. J. Viennot, G. Fève, B. Huard, C. Mora, A. Cottet, and T. Kontos, *Phys. Rev. Lett.* **107**, 256804 (2011).
- [6] T. Frey, P. J. Leek, M. Beck, A. Blais, T. Ihn, K. Ensslin, and A. Wallraff, *Phys. Rev. Lett.* **108**, 046807 (2012).
- [7] H. Toida, T. Nakajima, and S. Komiyama, *Phys. Rev. Lett.* **110**, 066802 (2013).
- [8] K. D. Petersson, L. W. McFaul, M. D. Schroer, M. Jung, J. M. Taylor, A. A. Houck, and J. R. Petta, *Nature* **490**, 380 (2012).
- [9] G. Deng, D. Wei, J. R. Johansson, M. Zhang, S. Li, H. Li, G. Cao, M. Xiao, T. Tu, G. Guo, H. Jiang, F. Nori, and G. Guo, *arXiv:1310.6118* (2013).
- [10] Y.-Y. Liu, K. D. Petersson, J. Stehlik, J. M. Taylor, and J. R. Petta, *Phys. Rev. Lett.* **113**, 036801 (2014).
- [11] P.-Q. Jin, M. Marthaler, J. H. Cole, A. Shnirman, and G. Schön, *Phys. Rev. B* **84**, 035322 (2011).
- [12] Y.-Y. Liu, J. Stehlik, C. Eichler, M. J. Gullans, J. M. Taylor, and J. R. Petta, *Science* **347**, 285 (2015).
- [13] B. Yurke and E. Buks, *J. Lightwave Technol.* **24**, 5054 (2006).
- [14] M. A. Castellanos-Beltran and K. W. Lehnert, *Appl. Phys. Lett.* **91**, 083509 (2007).
- [15] D. Bozyigit, C. Lang, L. Steffen, J. M. Fink, C. Eichler, M. Baur, R. Bianchetti, P. J. Leek, S. Filipp, M. P. da Silva, A. Blais, and A. Wallraff, *Nat. Phys.* **7**, 154 (2011).
- [16] C. Eichler, D. Bozyigit, and A. Wallraff, *Phys. Rev. A* **86**, 032106 (2012).
- [17] T. Hayashi, T. Fujisawa, H. D. Cheong, Y. H. Jeong, and Y. Hirayama, *Phys. Rev. Lett.* **91**, 226804 (2003).
- [18] J. Basset, D.-D. Jarausch, A. Stockklauser, T. Frey, C. Reichl, W. Wegscheider, T. M. Ihn, K. Ensslin, and A. Wallraff, *Phys. Rev. B* **88**, 125312 (2013).
- [19] C. Eichler, Y. Salathe, J. Mlynec, S. Schmidt, and A. Wallraff, *Phys. Rev. Lett.* **113**, 110502 (2014).
- [20] W. G. van der Wiel, S. De Franceschi, J. M. Elzerman, T. Fujisawa, S. Tarucha, and L. P. Kouwenhoven, *Rev. Mod. Phys.* **75**, 1 (2002).
- [21] M. Field, C. G. Smith, M. Pepper, D. A. Ritchie, J. E. F. Frost, G. A. C. Jones, and D. G. Hasko, *Phys. Rev. Lett.* **70**, 1311 (1993).
- [22] E. Buks, R. Schuster, M. Heiblum, D. Mahalu, and V. Umansky, *Physica B: Condensed Matter* **249 - 251**, 295 (1998).
- [23] L. Childress, A. S. Sørensen, and M. D. Lukin, *Phys. Rev. A* **69**, 042302 (2004).
- [24] Supplemental Material.
- [25] A. Wallraff, A. Stockklauser, T. Ihn, J. R. Petta, and A. Blais, *Phys. Rev. Lett.* **111**, 249701 (2013).
- [26] J. J. Viennot, M. R. Delbecq, M. C. Dartiailh, A. Cottet, and T. Kontos, *Phys. Rev. B* **89**, 165404 (2014).
- [27] C. Lang, D. Bozyigit, C. Eichler, L. Steffen, J. M. Fink, A. A. Abdumalikov Jr., M. Baur, S. Filipp, M. P. da Silva, A. Blais, and A. Wallraff, *Phys. Rev. Lett.* **106**, 243601 (2011).
- [28] T. Fujisawa, T. H. Oosterkamp, W. G. van der Wiel, B. W. Broer, R. Aguado, S. Tarucha, and L. P. Kouwenhoven, *Science* **282**, 932 (1998).
- [29] M. J. Gullans, Y. Y. Liu, J. Stehlik, J. R. Petta, and J. M. Taylor, *arXiv:1501.03499* (2015).
- [30] S.-H. Ou-Yang, C.-H. Lam, and J.-Q. You, *Chinese Physics B* **19**, 050519 (2010).
- [31] T. Fujisawa, D. G. Austing, Y. Tokura, Y. Hirayama, and S. Tarucha, *Nature* **419**, 278 (2002).
- [32] M. P. da Silva, D. Bozyigit, A. Wallraff, and A. Blais, *Phys. Rev. A* **82**, 043804 (2010).
- [33] C. Xu and M. G. Vavilov, *Phys. Rev. B* **88**, 195307 (2013).